Pile Side Resistance in Sands for the Unloading Effect and Modulus Degradation

C. F. Zhao[a], Y. Wu[a], C. Zhao[a,b],✉, Q. Z. Zhang[a], F. M. Liu[a], F. Liu[a]

a. Department of Geotechnical Engineering, Tongji University, (Shanghai, China)
b School of Engineering, Tibet University, Lhasa, (Tibet, China)
✉zhaocheng@tongji.edu.cn

ABSTRACT: A total of 36 groups of sand-concrete interface loading and unloading direct shear tests were used to analyze the mechanical properties of the pile side-soil interface. The test results show that the interface residual shear stress for the same applied normal stress tends to be constant for the rough sand-concrete interface. The initial shear modulus and peak shear stress of the interface both decrease with the degree of unloading and increase with the interface roughness. The maximum amount of interface shear dilatancy increases with the degree of unloading, and the maximum amount of interface shear shrinkage decreases with unloading for the same interface roughness. A pile side resistance-displacement model is established using the shear displacement method. The proposed function considers both the radial unloading effect and modulus degradation of soil around the pile. The effect of radial unloading and interface roughness on the degradation of the equivalent shear modulus is analyzed using a single fitting parameter b. Good agreement of the proposed model is confirmed by applying the direct shear tests of the 36 groups.

KEYWORDS: Concrete; Composite; Stability; Mechanical properties; Characterization

RESUMEN: *Resistencia de la superficie lateral del pilote a la descarga y a la degradación del módulo cortante en suelos arenosos.* Se han realizado 36 series de ensayos de corte directo con carga y descarga para analizar el comportamiento mecánico del interfaz entre la superficie del lateral del pilote y el suelo. Los resultados demuestran que al aplicar un determinado esfuerzo normal, el esfuerzo cortante residual en el interfaz rugoso entre el suelo arenoso y el hormigón tiende a ser constante. Tanto el módulo cortante inicial como el esfuerzo de cizalla máximo disminuyen al incrementar el grado de descarga y aumentan con la rugosidad del interfaz. Dada una misma rugosidad interfacial, el esfuerzo cortante interfacial máximo crece más rápidamente y su reducción máxima disminuye más lentamente al aumentar el grado de descarga. Se ha empleado el «método del desplazamiento del esfuerzo cortante» para desarrollar un modelo que describe la relación entre la resistencia de la superficie lateral del pilote y el desplazamiento. La función propuesta tiene en cuenta tanto la influencia de la descarga radial como la degradación del módulo cortante del suelo que rodea el pilote. Se analiza la influencia de la descarga radial y la de la rugosidad del interfaz sobre la degradación del módulo cortante equivalente mediante un solo parámetro de ajuste, b. Se ha confirmado que el acuerdo entre el modelo y los datos empíricos de los ensayos de corte directo de las 36 series analizadas es bueno.

PALABRAS CLAVE: Hormigón; Composite; Estabilidad; Propiedades mecánicas; Caracterización.

ORCID ID: C. F. Zhao (https://orcid.org/0000-0002-0010-1819); Y. Wu (https://orcid.org/0000-0002-8366-9871); C. Zhao (https://orcid.org/0000-0002-8973-9164); Q. Z. Zhang (https://orcid.org/0000-0002-7007-5871); F. M. Liu (https://orcid.org/0000-0002-5517-162X); F. Liu (https://orcid.org/0000-0001-9349-2400)

1. INTRODUCTION

Piles are generally used to transfer loads from the superstructure to a competent soil or rock layer (1). The use of pile side resistance analyses is becoming more important compared to solely using bearing capacity analyses. Extensive effort has been expended to develop theoretical methods to analyze pile side resistance behavior. These methods fall into four categories: (*i*) the load transfer method (1–3), which uses the pile side load-transfer function to describe the relationship between pile side resistance and pile-soil interface displacement; (*ii*) the shear displacement method (4–9), which assumes that the vertical displacement of the soil at any point around the pile is only related to the shear stress at this point and consider the vertical displacement of the soil induced by the shaft shear stress as a logarithmic relationship of the radial distance away from the pile side; (*iii*) the elastic theory method (10–12), which employs the Mindlin solution under the concentrated load in the elastic half-space to calculate the displacement of the soil. The equilibrium equation is established by the coordination conditions between the displacement of the pile body and soil to obtain the displacement and side resistance of the pile; (*iv*) the numerical analysis method (13–18), which includes the finite element method (17), boundary element method (13), discrete element method (16) and infinite layer method (14), and generally needs high computational requirements that caused them are not commonly used in practice.

The shear displacement method assumes that the vertical displacement of the soil at any point around the pile is only related to the shear stress at this point, the shear stress transfer causes the settlement of the surrounding soil, and thus the stress and deformation characteristics of the pile-soil system can be obtained (19). Although the conventional shear displacement method has some defects. For example, this method cannot reflect the pile side resistance softening phenomenon (20), but it is still widely used in the analysis of pile side load transfer mechanism due to its easy calculation process and theoretically reflecting the shear deformation properties of the soil around the pile. (7–8) derived the pile side resistance-displacement functions based on the shear displacement method. Guo et al. (21) modified the pile side resistance-displacement functions that derived from the shear displacement, considering the variations of soil stiffness and limiting pile side resistance with depth. Zhu at al. (22) considered the nonlinear elastic properties and modulus degradation characteristics of the soil into the pile side resistance-displacement functions. The stress-strain behavior of natural soils during shear is highly nonlinear, and the elastic modulus generally decreases with increase in shear strain (22).

On one hand, although above scholars considered many factors that affect the pile side resistance developed, the soil radial unloading for the non-displacement pile during boring stage almost has never been addressed. On other hand, the mechanical properties of soil around a non-displacement pile are very different compared with those of loading soil (23, 24). In particular, the radial unloading effect and modulus degradation characteristics of the soil are not considered comprehensively to a great degree in the pile side resistance-displacement model. As a result, it is difficult to quantify the radial unloading effect of the soil around the pile side on the pile side resistance developed through the field full scale pile tests. Furthermore, the static field full scale pile load tests are extensive and time-consuming although it is the most reliable means of assessing a single pile load transfer mechanism (25). However, the indoor model test has the advantages of parameter control, test repeatability, and lower cost (26). Hence, it can be achieved through the concrete-soil interface large direct shear tests to simulate the radial unloading during the boring stage and pile side-soil shear process (27).

In this paper, a series of sand-concrete interface loading and unloading direct shear tests are used to analyze the mechanical properties of the pile side-soil interface. First, the effect of the unloading process and interface roughness on the mechanical properties of the interface are discussed. Then, a pile side resistance-displacement model is established using the shear displacement method. The proposed τ–s function considers the effect of radial unloading during the non-displacement pile boring stage and modulus degradation of soil around the pile. The direct shear test data is used to validate the proposed model. At the end of this paper, the effect of radial unloading and sand-concrete interface roughness on the degradation of the equivalent shear modulus G_{eq} is analyzed using a single fitting parameter b.

2. LARGE DIRECT SHEAR TEST

2.1. Test apparatus

Although the large-scale direct shear apparatus has some inherent defects, it is frequently used in interface research due to its simplicity in principle and operation. The test apparatus used in this experiment is the large-scale multi-function direct shear test apparatus SJW-200, which is independently researched and developed by Tongji University, Shanghai, China. The test apparatus has a large size shear box with net size 600 mm × 400 mm × 200 mm (length × width × height) and wall thickness of 40 mm. The test apparatus in both the normal and tangential directions is equipped with an advanced

server and control system; the range of the test displacement and applied load are enough to satisfy the requirements of this paper. Compared with a conventional direct shear device, this test apparatus has more accurate test results because it can effectively reduce the boundary effect (7). Figure 1 is the schematic diagram of the large-scale direct shear test apparatus.

2.2. Soil specimen

The soil specimen was gray silt, which was obtained from a construction project in Shanghai City. The main properties of the soil are listed in Table 1; the grain-size distribution of the soil is shown in Figure 2.

2.3. Concrete plate specimen

Because the bored pile side surface is not smooth in actual engineering, it is necessary to consider the influence of the physical form of the sand-concrete interface. The key is how to simulate and define the roughness of the concrete plate. The quantitative criteria for the interface roughness are as follows.

Dove et al. (28) proposed using the surface regular sawtooth to quantify the soil-concrete interface roughness, as shown in Figure 3. The roughness of the interface can be changed by changing the sawtooth angle, height and space position relationship.

Zhang et al. (29), (30) proposed using the peak-to-valley distance R to quantify the steel plate interface roughness, as shown in Figure 4. The interface roughness can be changed by changing the peak-to-valley distance.

Considering the advantages and disadvantages of the above interface roughness definition and the actual situation of the pile wall, the interface
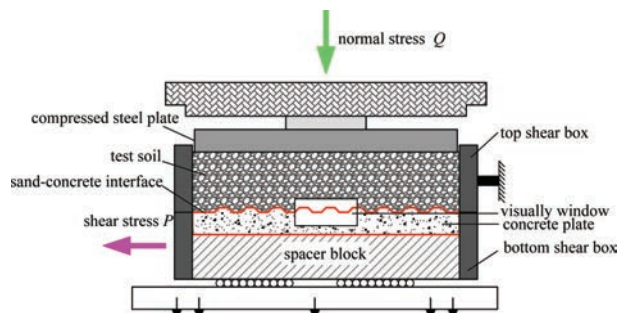
roughness model chosen in this paper is shown in Figure 5. Figure 5 shows that the shape of the rough concrete plate surface is a standard tooth, and its profile is trapezoidal. The tooth angle $\alpha = 45°$ remains constant, and the length of the bottom edge S_2 of the trapezoidal convex portion is equal to the bottom edge S_3 of the trapezoidal
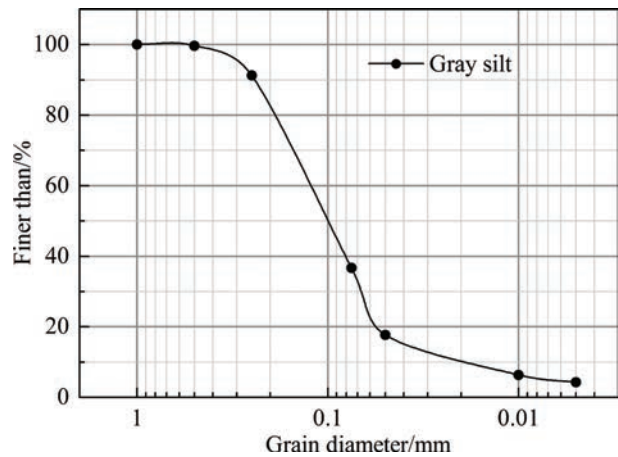

FIGURE 2. Grain-size distribution of gray silt soil (accumulative granulometrical grapher).
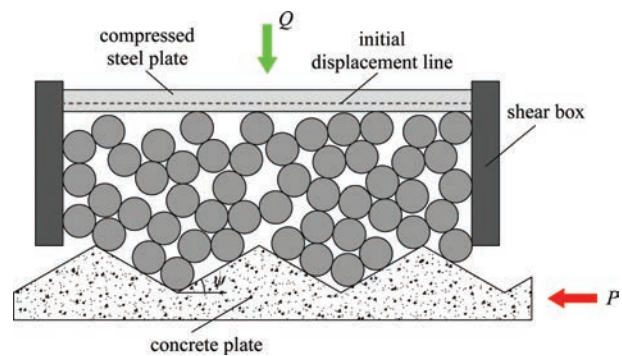

FIGURE 3. Illustration of the interaction between soil particles and a concrete plate (after (28)).
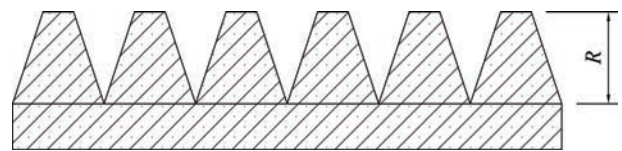

FIGURE 4. Illustration of the rough steel plate shape and the definition of roughness (after (29), (30)).

FIGURE 1. Schematic of the large direct shear apparatus.

TABLE 1. Parameters of the silt in tests.

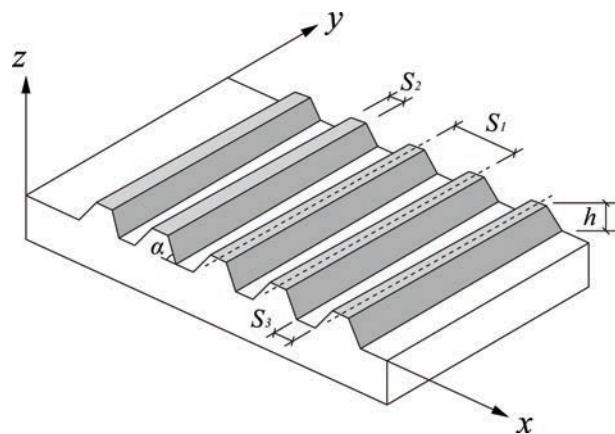| Unit weight $\gamma/(kN·m^{-3})$	Cohesion c/kPa	Internal friction angle $\varphi/(°)$	Water content $\omega/\%$	Void ratio e	Compression modulus E_{S1-2}/MPa
19.5	4	31.5	20	0.754	11.23

FIGURE 5. Illustration of the interface roughness model in this paper.

concave portion. The volume of the concave portion is always equal to the convex portion. By changing the tooth height h and keeping the other conditions unchanged, including tooth angle, space position relationship and so on, the roughness of the concrete plate interface can be adjusted. Hence, the interface roughness R can be expressed by the size of h.

Three variations of concrete plates are used in this experiment, namely, $R = 0$ mm, 10 mm and 20 mm according to the above definition of concrete interface roughness model. The concrete plate for testing was 600 mm long by 400 mm wide by 50 mm thick and is made of C25 concrete, and bidirectional bars with a diameter of $\varphi 8$ @ 100 are added into it.

2.4. Test procedures

A total of 36 groups of sand-concrete interface direct shear tests with three different degrees of interface roughness and initial normal stress were used. The test soil is first consolidated under an initial normal stress σ_c for 1 hour and then unloaded to a specific applied normal stress σ_s to shear. Both the loading and unloading rates are 0.5 kPa/s. The three programs of loading and unloading for three different roughness of concrete-soil interface are: (i) $\sigma_c = 300$ kPa, and $\sigma_s = 300$, 250, 200, 150, 100, 50 kPa, respectively; (ii) $\sigma_c = 200$ kPa, and $\sigma_s = 200$, 150, 100, 50 kPa, respectively; (iii) $\sigma_c = 100$ kPa, and $\sigma_s = 100$, 50 kPa, respectively. The shear stage begins when the curve of the normal displacement to time is stable, which means the normal displacement is less than 0.001 mm within 1 minute under the applied normal stress. The shear rate is controlled at a constant rate of 2 mm/min. All data regarding the test are collected by a computerized data logging system; the results are monitored and saved using the computer software TEST.

3. TEST RESULTS ANALYSIS

3.1. Effect of loading and unloading on the sand-concrete interface mechanical properties

Figure 6 shows the interface shear stress-shear displacement curves for different initial and applied normal stresses to study the effect of loading and unloading on the interface mechanical properties. For the sake of simplicity, the legend is expressed as initial normal stress σ_c-applied normal stress σ_s. For example, the legend showing 300–100 means the interface is consolidated at the initial normal stress of 300 kPa, and sheared at the applied normal stress of 100 kPa. Figure 6 also shows that the interface peak shear stress τ_f increases with the initial normal stress under the unloading conditions when the interface roughness $R = 0$ mm and 10 mm, but both τ_f are less than the loading conditions. For $R = 20$ mm, the interface peak shear stress increases with the initial normal stress. For the rough soil-concrete interface, the interface residual shear stress tends to be a constant regardless of the loading and unloading conditions and increases with the interface roughness. However, the interface residual shear stress tends to be a constant only for the unloading condition in the smooth soil-concrete interface.

The above can be explained by these points. Higher initial normal stress contributes to a higher density of the interface, which results in soil particles around the interface needing a higher shear stress to make them move along the roughness interface and each other. Therefore, interface peak shear stress increases with the initial normal stress at high roughness. If the interface roughness is low, the interface peak shear stress is mainly influenced by the water content of the interface soils rather than the density. Higher initial normal stress lowers the water content of the interface soils, and if the water content is below the optimal water content, the interface peak shear stress under unloading may be less than the loading condition.

The shapes of the curves for loading and unloading are both logarithmic, and the strain softening phenomena of the curves are also consistent between loading and unloading. These phenomena show that the effect of loading and unloading on the sand-concrete interface mechanical properties change the value of interface peak shear stress, but there is no fundamental change in the failure mode of the interface.

3.2. Effect of unloading degree on the sand-concrete interface mechanical properties

Figure 7 shows the shear stress-shear displacement curves for the initial normal stress at 300 kPa unloaded with different applied normal stress to shear. The unloading degree is defined as the ratio
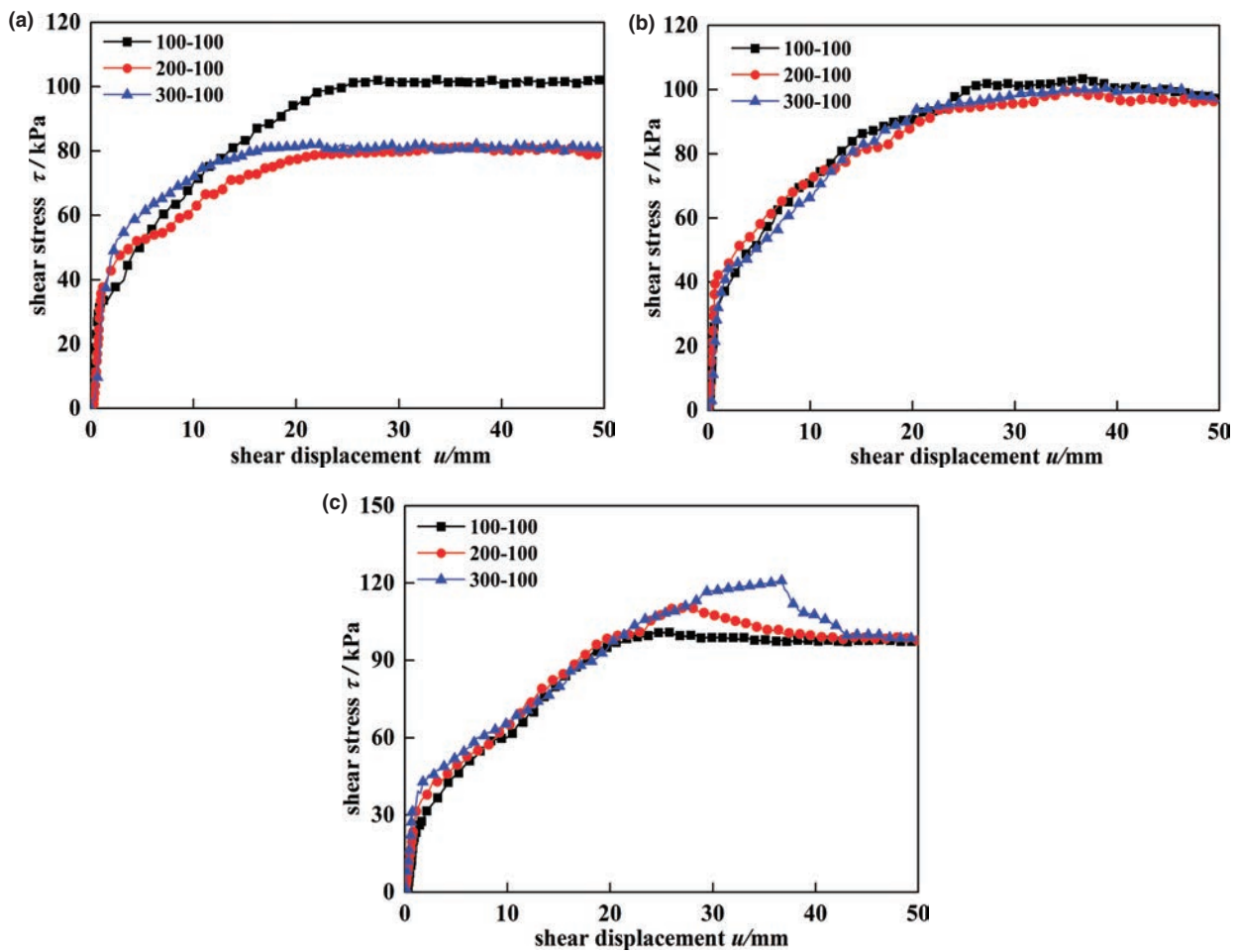
FIGURE 6. Curves of shear stress-shear displacement for loading and unloading conditions:
(a), (b) and (c) show the interface roughness at 0 mm, 10 mm and 20 mm, respectively.

of the increment between the initial and applied normal stress to the initial normal stress. Figure 7 also shows that the unloading degree has a significant effect on the sand-concrete interface mechanical properties. The peak shear stress, the shear displacement corresponding to the peak shear stress and the interface initial shear modulus G_0 all decrease with the unloading degree for the same interface roughness R.

3.3. Effect of interface roughness on the sand-concrete interface mechanical properties

Figure 8 shows the fitting curves between peak shear stress and applied normal stress for different interface roughness and initial normal stress. Table 2 shows the interface equivalent frictional angle φ calculated from the fitting curves. Figure 8 and Table 2 also show that the interface equivalent friction angle φ increases positively with roughness for the same initial normal stress; the rate of

increase is positive with the initial normal stress. The interface equivalent friction angle φ is mainly affected by the interface roughness and the initial normal stress.

3.4. Effect of loading and unloading on the sand-concrete interface shear dilatancy and shrinkage

Figure 9 shows the variation curves of maximum interface, shear dilatancy and shrinkage amount for different conditions. In this paper, the sign of normal displacement corresponding to the interface shear dilatancy is negative, and the sign of normal displacement corresponding to the interface shrinkage is positive. Figure 9 also shows that the maximum amount of interface shear dilatancy decreases with the applied normal stress σ_s, while the maximum amount of interface shear shrinkage increases with the applied normal stress σ_s as the σ_s increases to a value for the same interface roughness and initial normal stress. The maximum amount
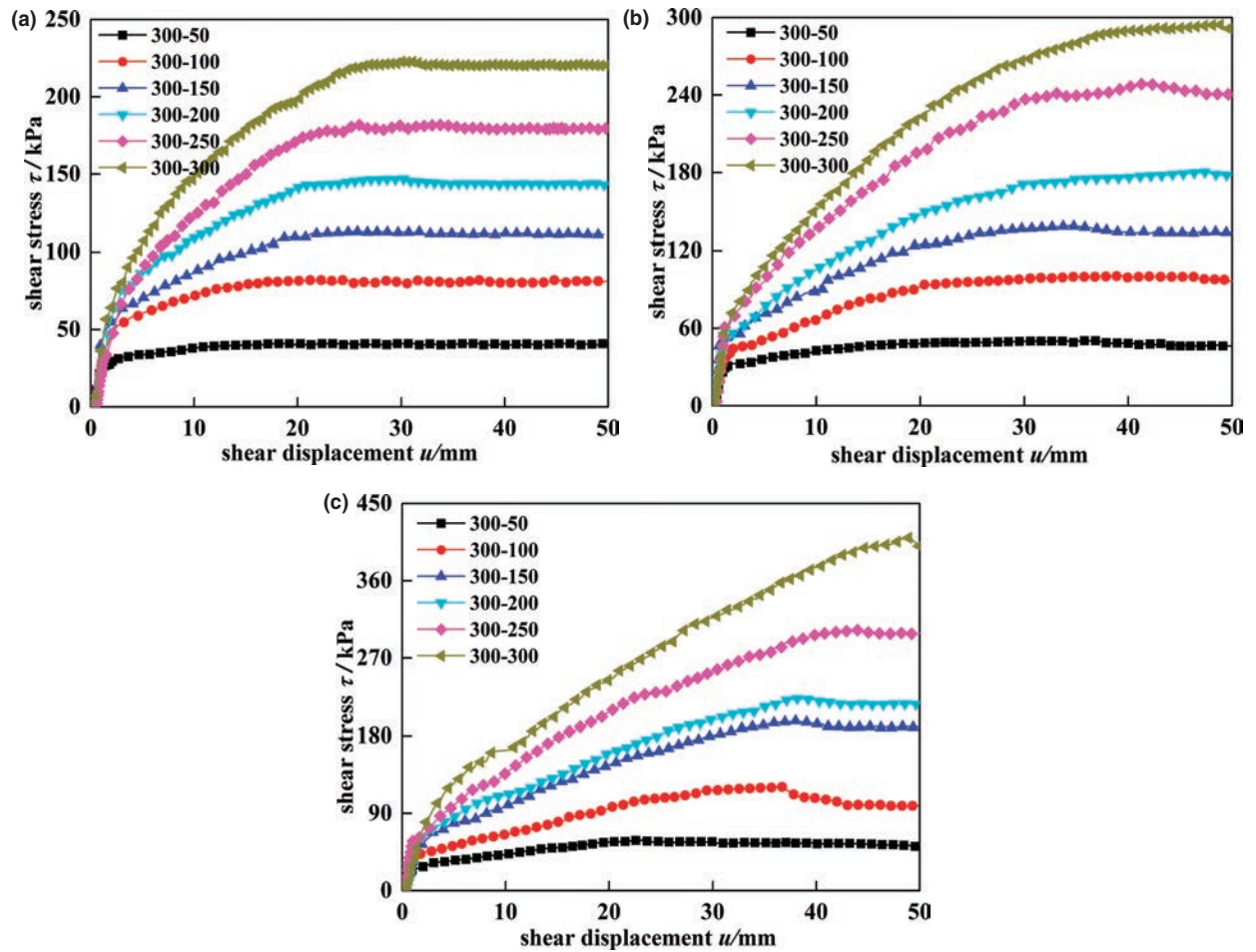
FIGURE 7.   Curves of shear stress-shear displacement for different unloading degree conditions: (a), (b) and (c) show the interface roughness at 0 mm, 10 mm and 20 mm, respectively.

of interface shear dilatancy increases with the initial normal stress, and the maximum amount of interface shear shrinkage decreases with the initial normal stress for the same interface roughness and applied normal stress.

4. MODEL DESCRIPTION

The proposed pile side resistance-displacement model curve, as shown in Figure 10, consists of two parts: (*i*) a nonlinear pre-failure portion and (*ii*) a perfectly plastic after-failure portion. Figure 10 shows that the pile side resistance increases nonlinearly with the pile-soil interface displacement increased at first. When the pile-soil interface displacement reaches the value s_u, the pile side resistance achieves its peak value τ_f. The pile side resistance will keep the fixed value τ_f with the pile-soil interface displacement increased. The softening or hardening behavior of the soil, as illustrated in Figure 10, is not considered in this paper.

4.1. Theory function of pile side resistance-displacement

The vertical displacement of the soil at any point around the pile is only related to the shear stress at this point, according to the shear displacement method assumptions, and can be expressed as [1] (19):

$$s(z) = f(\tau_s) \qquad [1]$$

where $s(z)$ is the vertical displacement of the soil at a point where the depth is z; τ_s is the shear stress of the soil at that point.

Randolph et al. (7) proposed an approximate analytical solution for the pile side resistance-displacement based on the shear displacement method and expressed the solution as [2]:

$$s(z) = \tau_0 r_0 \int_{r_0}^{r_m} \frac{dr}{r \cdot G(\tau_s, r)} \qquad [2]$$
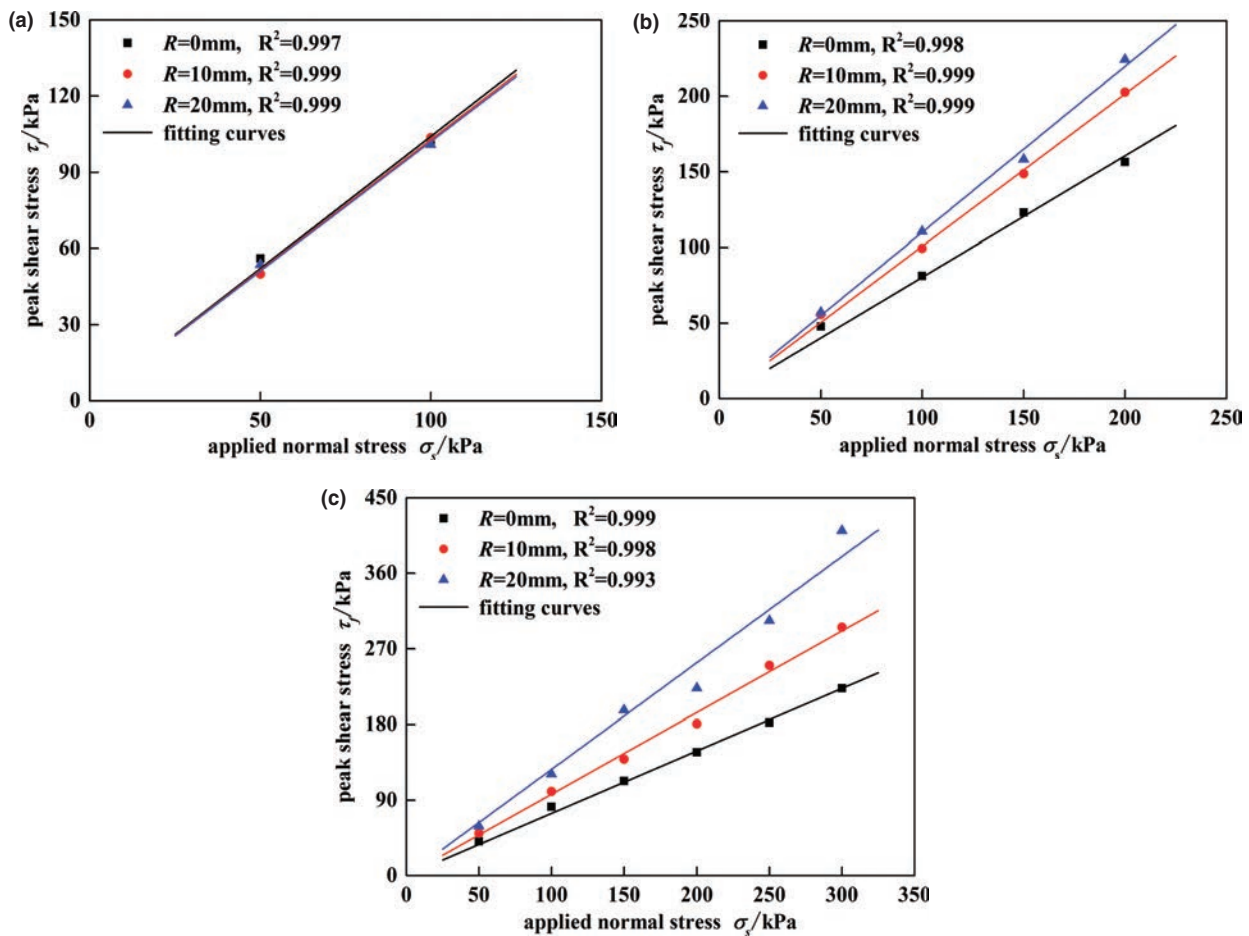
FIGURE 8.   Fitting curves of peak shear stress and applied normal stress for different roughness conditions: (a), (b) and (c) show the initial normal stress at 100 kPa, 200 kPa and 300 kPa, respectively.

TABLE 2. The interface equivalent frictional angle φ for different roughness and initial normal stress.

Roughness R /mm	Initial normal stress /kPa		
	100	200	300
0	45.7°	46.5°	47.1°
10	38.4°	44.5°	47.7°
20	36.5°	43.3°	51.7°

where r_0 and r_m are the radius of the pile and the limiting radius where the shear stress becomes negligible, respectively; τ_0 and $G(\tau_s, r)$ are the shear stress of the pile side and the shear modulus of the soil mass, respectively.

Soil Modulus Degradation

The stress-strain behavior of most geomaterials is highly nonlinear at all phases of loading (22). There is a significant reduction in stiffness with increasing strain level. The larger value of soil shear strain, the lower value of soil shear modulus during the shearing process. According to the assumptions of the shear displacement method, the shear strain of the soil around the pile is decreased with the radial distance from the pile increased. Hence, the degradation model of the soil shear modulus $G(\tau_s, r)$ along the pile radial direction can be assumed in Figure 11. The equation of the soil shear modulus $G(\tau_s, r)$ is expressed as [3]:

$$\begin{cases} G(\tau_s, r) = G_{s0} \cdot \left[M + (1-M) \cdot \dfrac{r - r_0}{r_1 - r_0} \right] & (r_0 \le r < r_1) \\ G(\tau_s, r) = G_{s0} & (r \ge r_1) \end{cases} \quad [3]$$

where r_1 represents the turning point where the soil shear modulus $G(\tau_s, r)$ begins to degenerate and the value of $r_1 \le r_m$; M represents the soil shear modulus degradation coefficient.
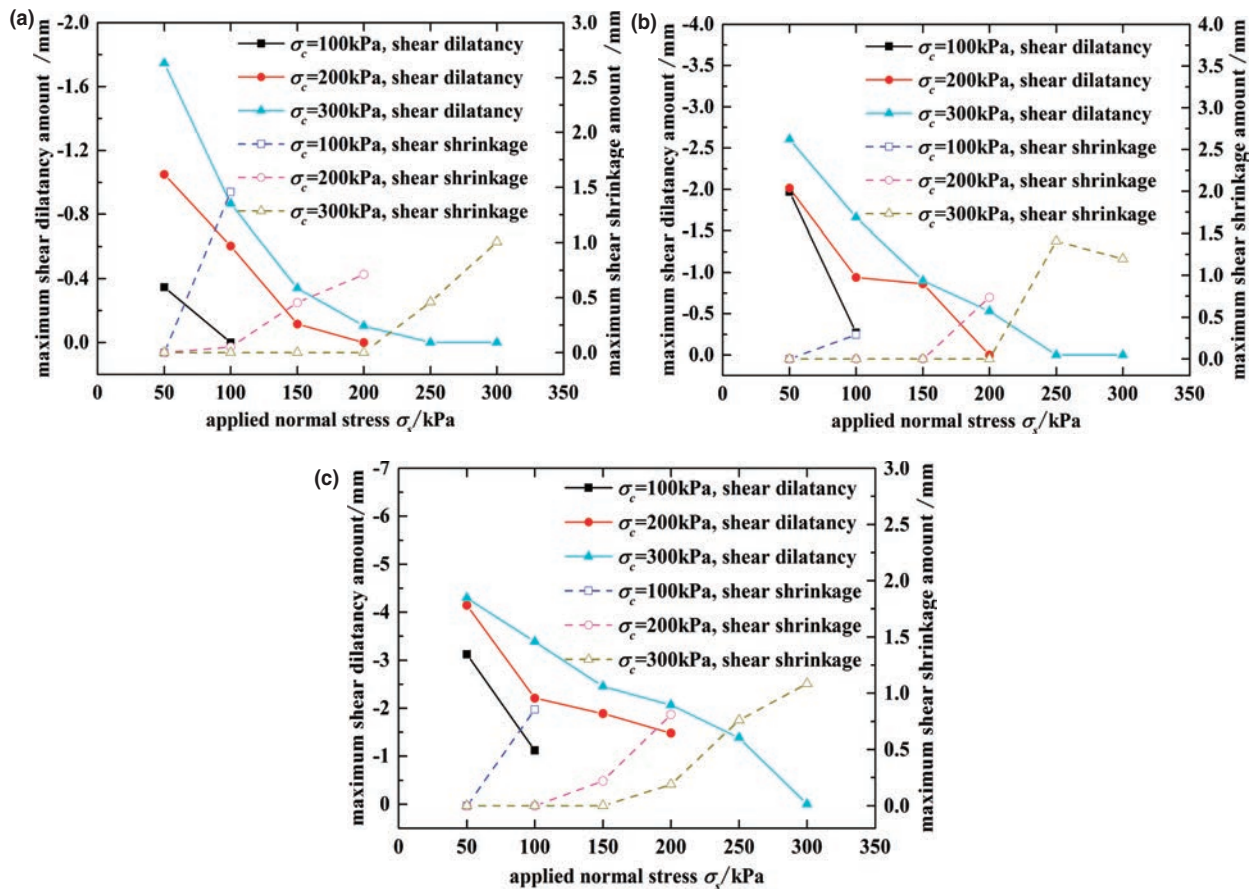
FIGURE 9.   Variation curves of maximum interface shear dilatancy and shrinkage amount for different conditions: (a), (b) and (c) show the interface roughness at 0 mm, 10 mm and 20 mm, respectively.

By introducing Eq. [3] into Eq. [2] and integrating them, Eq. [2] becomes [4]:

$$s(z) = \tau_0 r_0 \left(\int_{r_0}^{r_1} \frac{dr}{r \cdot G_{s0} \cdot \left[M + (1-M) \cdot \frac{r-r_0}{r_1-r_0} \right]} + \int_{r_1}^{r_m} \frac{dr}{r \cdot G_{s0}} \right) \quad [4]$$

The concept of equivalent shear modulus G_{eq} is adopted to facilitate the solution of Eq. [4] where the shear modulus varying in Eq. [4] is equivalent to a constant shear modulus G_{eq} expressed as [5] and [6]:

$$s(z) = \tau_0 r_0 \left(\int_{r_0}^{r_1} \frac{dr}{r \cdot G_{s0} \cdot \left[M + (1-M) \cdot \frac{r-r_0}{r_1-r_0} \right]} + \int_{r_1}^{r_m} \frac{dr}{r \cdot G_{s0}} \right)$$

$$= \frac{\tau_0 r_0}{G_{eq}} \int_{r_0}^{r_m} \frac{dr}{r} \quad [5]$$

$$G_{eq} = \frac{\int_{r_0}^{r_m} \frac{1}{r} \cdot dr}{\int_{r_0}^{r_1} \frac{1}{r \cdot G_{s0} \cdot \left[M + (1-M) \cdot \frac{r-r_0}{r_1-r_0} \right]} \cdot dr}$$

$$+ \int_{r_1}^{r_m} \frac{1}{r \cdot G_{s0}} \cdot dr \quad [6]$$

The shear modulus $G(\tau_s, r)$ (or G_{eq}) is related to the soil shear stress τ_s around the pile (or pile side resistance τ_0) and soil initial shear modulus G_{s0}. Fahey et al. (31) proposed a modified hyperbolic model to express the degradation of soil sear modulus $G(\tau_s, r)$ expressed as [7]

$$\frac{G(\tau_s, r)}{G_{s0}} = 1 - a \cdot \left(\frac{\tau_s}{\tau_{max}} \right)^b \quad [7]$$

where the coefficient a and b are the degree and rate, respectively, of the shear modulus degradation.
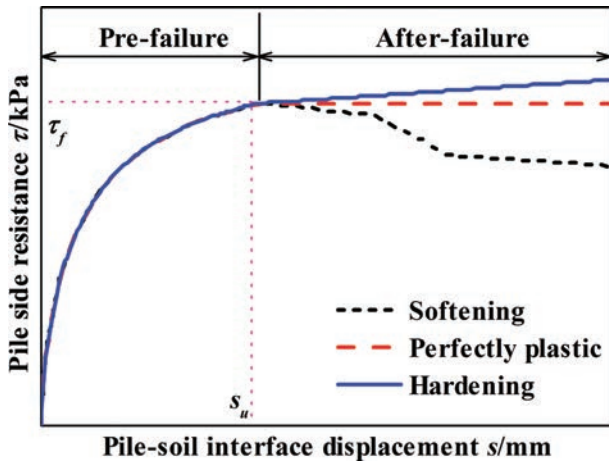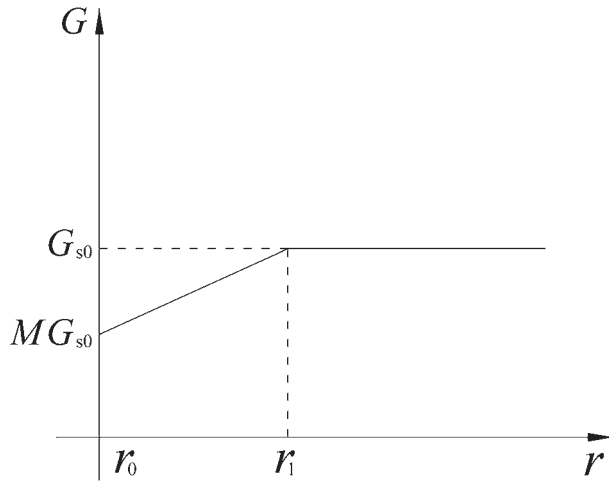
FIGURE 10.   Schematic of the proposed model.

FIGURE 11.   Degradation model of the G (τ_s, r).

τ_s and τ_{max} are the soil shear stress and maximum soil shear stress around the pile. For the equivalent shear modulus G_{eq}, it is necessary to replace the τ_s and τ_{max} of the pile side resistance τ_0 and peak pile side resistance τ_f in Eq. [7], expressed as [8]

$$\frac{G_{eq}}{G_{s0}} = 1 - a \cdot \left(\frac{\tau_0}{\tau_f}\right)^b \qquad [8]$$

By introducing Eq. (8) into Eq. (5) and integrating them, Eq. [5] becomes [9]

$$s(z) = \frac{\tau_0 \cdot r_0}{G_{s0} \cdot \left[1 - a \cdot \left(\frac{\tau_0}{\tau_f}\right)^b\right]} \cdot \ln(r_m / r_0) \qquad [9]$$

Evaluation of Peak Pile Side Resistance τ_f

There are three methods for determining the peak pile side resistance τ_f: (i) the α method belonging to the total stress method (32); (ii) the β method belonging to the effective stress method (33); and (iii) the λ method belonging to the mixing method (34). For the object of this paper, the β method is modified to determine the peak pile side resistance τ_f considering the unloading effect.

The β method can be used to calculate the pile side resistance of both cohesive soil and non-cohesive soil. It was proposed by Chandler et al. (33), and the calculated formula is expressed as [10]

$$\tau_f = \sigma'_v \cdot K_0 \cdot \tan\delta = \beta \cdot \sigma'_v \qquad [10]$$

where σ'_v is the average vertical effective stress of the pile side-soil layer; K_0 is the static lateral pressure coefficient; δ is the pile-soil interface friction angle.

For normal consolidated soil, $K_0=1-\sin\varphi'$, where φ' is the effective internal friction angle of the soil δ=φ', and $\beta = (1- \sin\varphi')\cdot\tan\varphi'$. For over-consolidated soil, the effect of over-consolidation OCR should be considered. Mayne et al. (35) proposed a modified formula for calculating the value of β for over-consolidated soil [11]

$$\beta = (1 - \sin\varphi') \cdot \text{OCR}^{\sin\varphi'} \cdot \tan\delta \qquad [11]$$

The over-consolidation ratio OCR is calculated as [12]

$$\text{OCR} = \sigma_c / \sigma_s \qquad [12]$$

where σ_c and σ_s are the initial consolidation normal stress and applied normal stress in the process of shearing, respectively. The unloading ratio ξ is introduced when considering the unloading effect and is expressed as [13]

$$\xi = (\sigma_c - \sigma_s)/\sigma_c \qquad [13]$$

Introducing Eq. [11], Eq. [12] and Eq. [13] into Eq. [10] becomes [14]

$$\tau_f = (1 - \sin\varphi') \cdot (1 - \xi)^{-\sin\varphi'} \cdot \tan\delta \cdot \sigma'_v \qquad [14]$$

Eq. [22] is the peak pile side resistance calculation function that considering the unloading effect.

Evaluation of the influence area of radial limiting radius r_m

Randolph et al. (23) proposed the following equation as an estimation method to calculate the r_m [15]

$$r_m = C \cdot L \cdot \rho \cdot (1 - v) \qquad [15]$$

where C is the empirical coefficient, and its value is 2.5 for a pile in the semi-infinite space and 2.0 for the rigid layer below the pile end 2.5 times the pile length; L is the depth of the pile in the soil; ρ is the ratio of soil shear modulus at mid-depth to that at the pile tip, and $\rho = 1.0$ for uniform soil; v is the Poisson ratio, and its value generally takes v = 0.2 ~ 0.4 for Shanghai sand.

From Eq. [15], it is relatively simple to determine the r_m, but this equation does not consider the impact of the load level of the pile and the change of r_m with the pile buried depth. Hence, this paper uses the following method to determine the value of r_m.

The downward displacement of the soil at $r = r_m$ is 0, according to the shear displacement method assumptions. Thus, differentiating Eq. [2] on both sides is expressed as [16]

$$ds(z)\big|_{r=r_m} = \frac{\tau_0 r_0}{r_m \cdot G(\tau_s, r_m)} = \frac{\tau_0 r_0}{r_m \cdot G_{s0}} = 0 \qquad [16]$$

Eq. [16] shows that the hold condition is $r_m \to \infty$. In the actual engineering, it is impossible to meet the conditions of $r_m \to \infty$. Therefore, there exists a treatment measure as follows [17]

$$ds(z) = \frac{\tau_0 r_0}{r_m \cdot G_{s0}} = \eta \qquad [17]$$

where η is a finite small value. Solving r_m from Eq. (17) can be expressed as [18]

$$r_m = \frac{\tau_0 r_0}{\eta \cdot G_{s0}} \qquad [18]$$

Eq. [18] shows that the r_m is related to the pile side resistance τ_0 (reflecting the pile load level), the soil initial shear modulus G_{s0} (reflecting the soil properties) and the pile radius r_0 (reflecting the pile shape).

By introducing Eq. [14] and Eq. [18] into Eq. [9], the pile side resistance-displacement model considering the unloading effect and soil modulus degradation is obtained as follows [19]:

$$s(z) = \frac{\tau_0 \cdot r_0}{G_{s0}} \cdot \frac{\ln\left[\tau_0/(\eta \cdot G_{s0})\right]}{\left[1 - a \cdot \left(\dfrac{\tau_0}{\sigma'_v \cdot (1 - \sin\varphi') \cdot (1-\xi)^{-\sin\varphi'} \cdot \tan\delta}\right)^b\right]} \qquad [19]$$

4.2. Determination of the values of parameters a, b, η, δ and G_{s0}

Evaluation of Parameters a, b and η

The range of the coefficient a is from 0 to 1.0, and (36) suggests that the results of most cases can be well fitted when a = 0.98. Mayne et al. (37) suggests that the range of the coefficient b is from 0.2 to 0.4 for most types of soil. In this paper, the range of empirical coefficient b is extended to $b = 0.02 \sim 0.4$.

The value of parameter η can be obtained by experiment. Randolph et al. (7) suggests that the range of value for η is $1 \times 10^{-7} \sim 1 \times 10^{-5}$, its value can take 1×10^{-6}.

Evaluation of Parameters δ

The parameter δ is the pile-soil interface friction angle, and its value varies with the type of pile and soil properties and generally takes as Table 3 recommended.

Evaluation of Initial Soil Shear Modulus G_{s0}

The initial shear modulus of the soil G_{s0} is generally calculated by the E-v model in actual engineering [20]

$$G_{s0} = \frac{E}{2(1+v)} \qquad [20]$$

where E and v are the elastic modulus and Poisson's ratio of the soil, respectively. For Shanghai soil, $E = 3.5E_{s1-2}$ according to Wang et al. (39). v is the Poisson ratio, and its value generally is v = 0.2 ~ 0.4 for Shanghai sand.

4.3. Algorithm for analysis of the pile side resistance-displacement model

The algorithm for the analysis of the pile side resistance-displacement model can be summarized as follows:

1. The integral relation of τ-s function is derived by using the shear displacement method, as shown in Eq. [5].

TABLE 3.   Recommended interface friction angle (after (38)).

Pile material	δ
Rough concrete	φ'
Smooth concrete	$0.8\varphi'$ to φ'
Steel	$0.5\varphi'$ to $0.9\varphi'$
Timber	$0.8\varphi'$ to $0.9\varphi'$

2. The degradation model of the shear modulus is obtained by using the modified hyperbolic function, as shown in Eq. [8].
3. Solve the peak pile side resistance τ_f using Eq. [14].
4. Solve the limiting radius r_m using Eq. [18].
5. Obtain the formula of the pile side resistance-displacement model by introducing Eq. [8], Eq. [14] and Eq. [18] into Eq. [5], thus becoming Eq. [19].

5. MODEL VALIDATION AND ANALYSIS

The test results obtained by the large-scale direct shear test are used to validate the pile side resistance-displacement model. The parameter r_0 in Eq. [19] cannot be reflected in the direct shear test. The pile-soil interface shear strength τ_f can be derived directly from the test results and do not need to be calculated by Eq. [14]. Hence, Eq. [19] can be transformed as follows [21]

$$\frac{s}{r_0} = \frac{\tau_0}{G_{s0}} \cdot \frac{\ln\left[\tau_0/(\eta \cdot G_{s0})\right]}{\left[1 - a \cdot \left(\tau_0/\tau_f\right)^b\right]} \qquad [21]$$

where τ_0 and τ_f are the current shear stress and peak shear stress in the direct shear test, respectively. Using the parameter τ to replace τ_0 in Eq. [21], s is the shear displacement.

5.1. Comparison curves between the model calculation and test values with different σ_c

The curves of s/r_0-τ/τ_f are plotted and compared with the τ-s curves obtained by the large-scale direct shear test. The τ/τ_f -s/r_0 curves are plotted on the main coordinate axis, and the τ-s curves are plotted on the sub-coordinate axis. The main coordinate axis and sub-coordinate axis in the figure have strict correspondence. The curves of both model calculation and test values are the pre-failure portion; after-failure portion is not considered for it is assumed perfectly plastic. The range of empirical coefficient b is extended to $b = 0.02 \sim 0.4$.

Figures 12 a, b and c are the comparison curves for the interface roughness $R = 0$ mm and $\sigma_c = 100$ kPa, 200 kPa and 300 kPa, unloaded to $\sigma_s = 50$ kPa. Figure 12 shows that the test values fit well with the model calculation, and the value of empirical
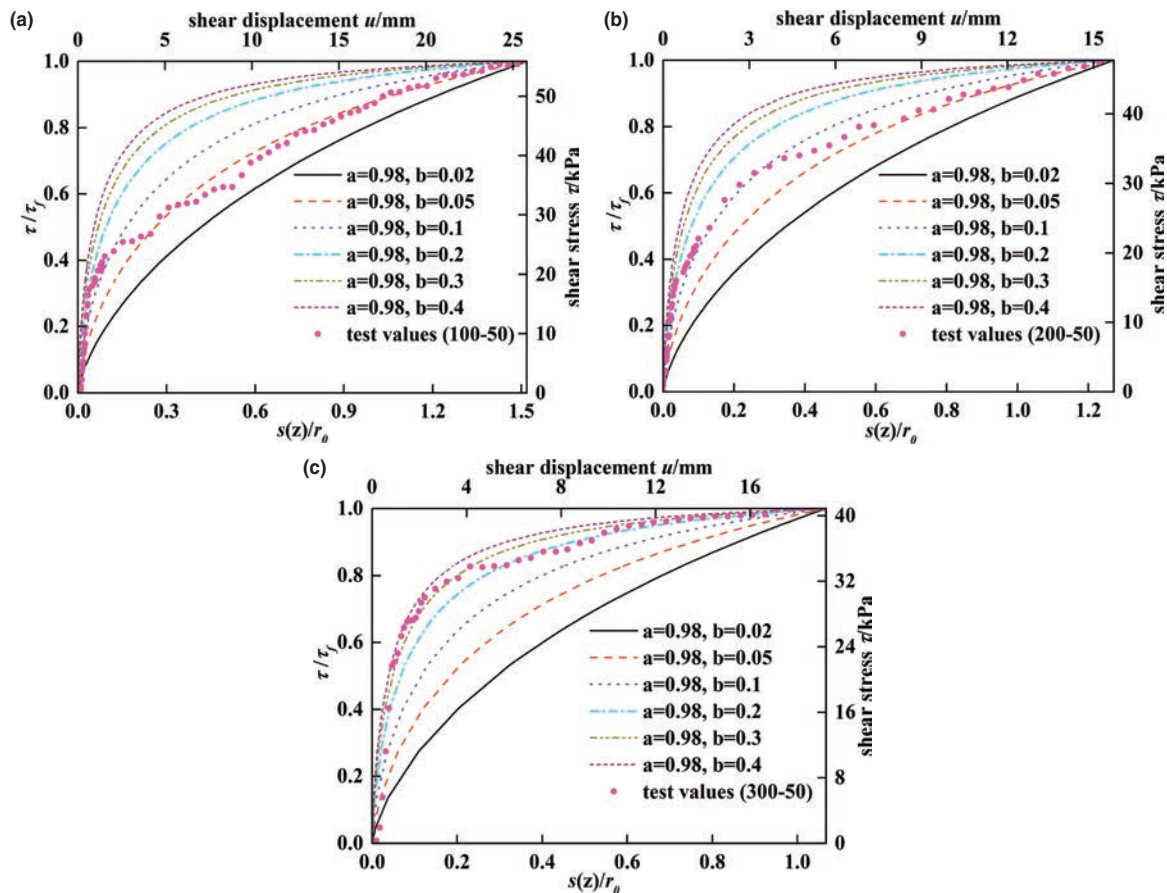

FIGURE 12.   Comparison curves of the model calculation and test values for $R = 0$ mm and $\sigma_s = 50$ kPa: (a), (b) and (c) are the initial normal stress $\sigma_c = 100$ kPa, 200 kPa and 300 kPa, respectively.

coefficient b gradually changed from 0.05 to 0.3 as the σ_c increased. This phenomenon shows that the value of empirical coefficient b increases positively with the initial normal stress σ_c in the same applied normal stress and interface roughness.

5.2. COMPARISON CURVES BETWEEN THE MODEL CALCULATION AND TEST VALUES UNDER DIFFERENT σ_S

Figures 13 a, b and c are the comparison curves for the interface roughness $R = 0$ mm and $\sigma_c = 300$ kPa unloaded to $\sigma_s = 300$ kPa, 200 kPa and 100 kPa, respectively. Figure 13 show that the test values in the loading conditions fit the best with the model calculation values when the empirical coefficient $a = 0.98$ and $b = 0.05$. The test curves that fit with the model calculations gradually shift up with unloading degree increase; the value of empirical coefficient b is gradually changed from 0.05 to 0.2 with the unloading degree increased. This phenomenon shows that the value of empirical coefficient b increases with the unloading degree increased.

5.3. Comparison curves between the model calculation and test values under different R

Figures 14 a and b, and Figures 15 a and b are both the comparison curves of the interface roughness $R = 10$ mm and $R = 20$ mm, respectively. Figure 14 (a) ~ (b) show that the test values fit best with the calculated values at $b = 0.05\sim0.1$ for $R = 10$ mm and $b = 0.02$ for $R = 20$ mm, respectively. Figures 15 a and b show that b = 0.1~0.2 and b = 0.05~0.1 for $R = 10$ mm and $R = 20$ mm, respectively. Combined with Figures 13 b and c, Figure 14 and Figure 15 show that the value of empirical coefficient b decreases with interface roughness.

5.4. Effect of unloading and roughness on the equivalent shear modulus degradation

Figure 16 shows the degradation curves of the equivalent shear modulus G_{eq}, which is calculated from the modified hyperbolic function given by Eq. (8) where $a = 0.98$ and b is 0.02 to 1. Figure 16 shows that the degradation rate of G_{eq} decreases with the
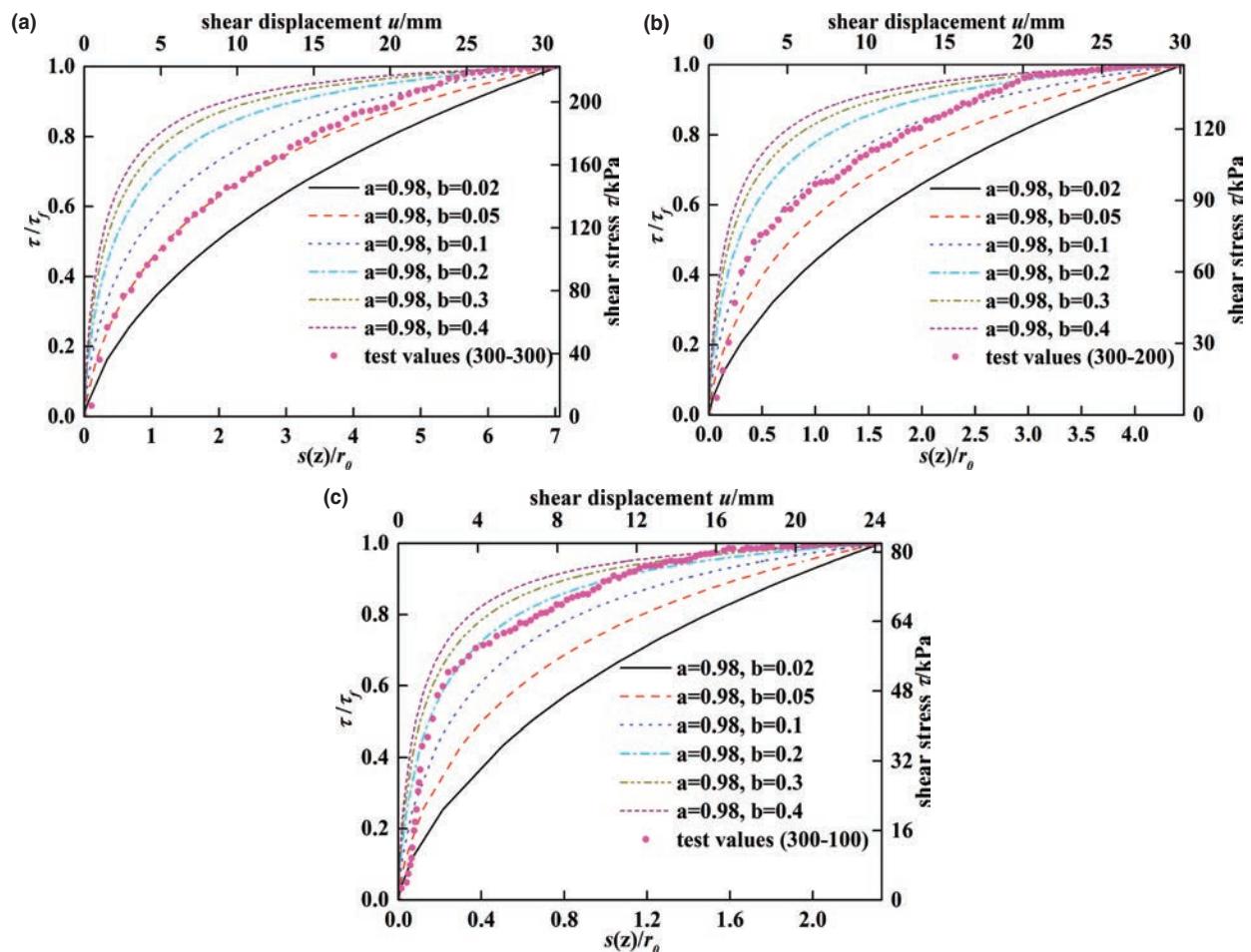

FIGURE 13. Comparison curves of the model calculation and test values under $R = 0$ mm and $\sigma_c = 300$ kPa: (a), (b) and (c) are the applied normal stress $\sigma_s = 300$ kPa, 200 kPa and 100 kPa, respectively.
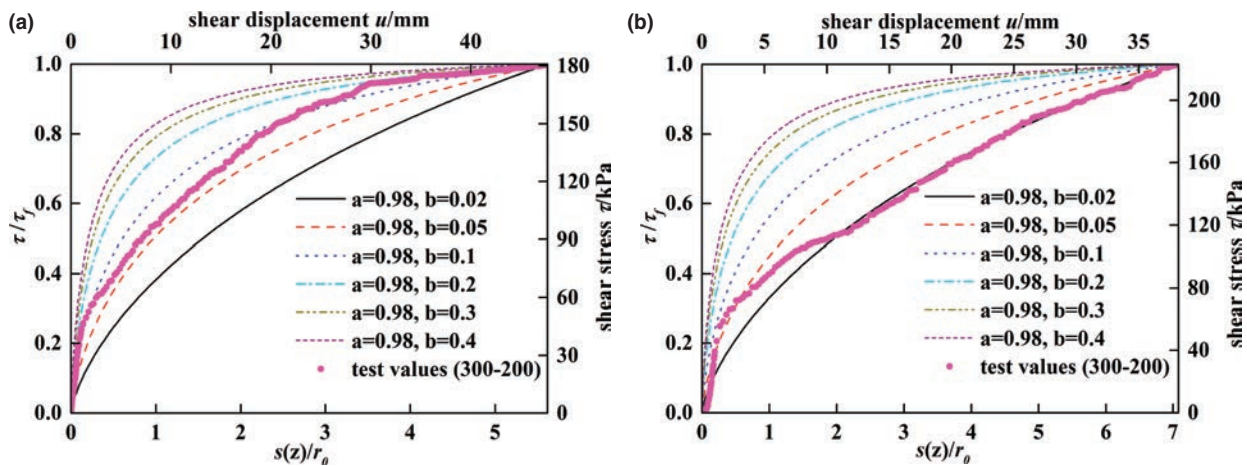
FIGURE 14. Comparison curves of the model calculation and test values for σ_c = 300 kPa and σ_s = 200 kPa: (a) and (b) show the interface roughness at 10 mm and 20 mm, respectively.
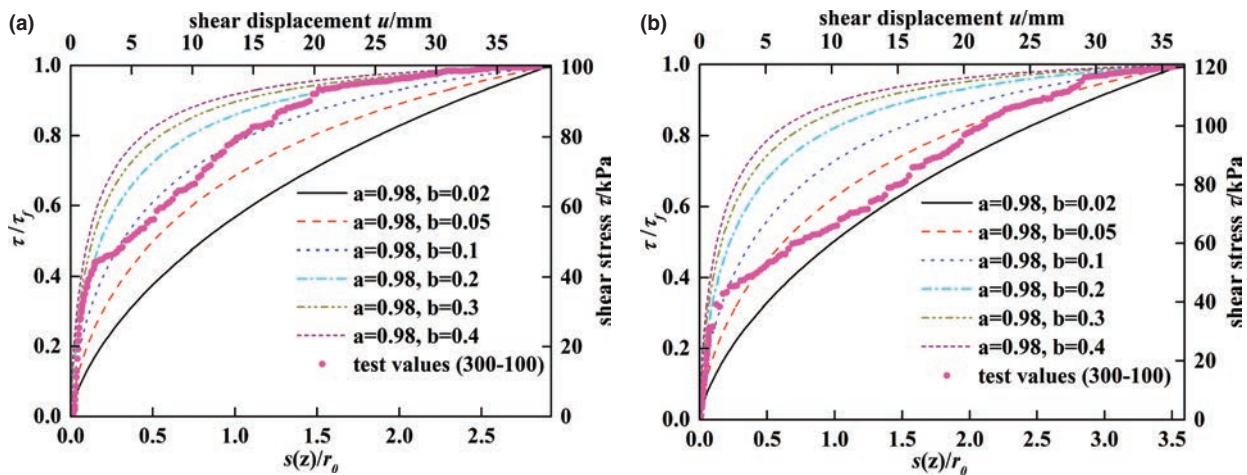

FIGURE 15. Comparison curves of the model calculation and test values for σ_c = 300 kPa and σ_s = 100 kPa: (a) and (b) show the interface roughness at 10 mm and 20 mm, respectively.
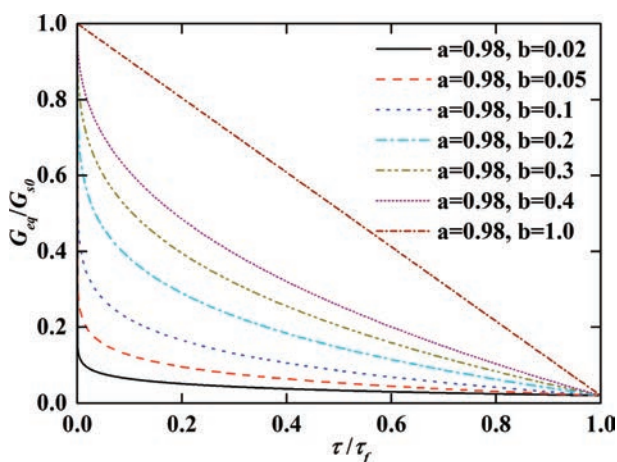

FIGURE 16. Degradation curves of the equivalent shear modulus.

value of b during the early shearing stage (about $\tau < 0.05\tau_f$) and increases with the value of b after the early shearing stage.

The above analysis (section 5.1 to 5.3) shows that the value of the empirical coefficient b increases with the unloading degree but decreases with interface roughness. Unloading will slow down the degradation of G_{eq} during the early shearing stage; the degradation rate of G_{eq} decreases with the unloading degree. After the early shearing stage, unloading accelerates the degradation of G_{eq}; however, the effect of interface roughness on the degradation of G_{eq} is opposite to the unloading degree. The increase of interface roughness will accelerate the degradation of G_{eq} during the early shearing stage and decelerate the degradation of G_{eq} after the early shearing stage.

6. CONCLUSIONS

In this study, large scale direct shear tests are conducted to analyze the mechanical properties of the pile side-soil interface. The effects of the unloading process and interface roughness on the mechanical properties of the interface are discussed. A pile side resistance-displacement model is developed using the shear displacement method. The proposed function considers both the radial unloading effect and modulus degradation of soil around the pile. The main conclusions are drawn as follows:

(1) The shapes of the interface shear stress-displacement curves for loading and unloading are both logarithmic and the effect of loading and unloading on the sand-concrete interface mechanical properties mainly change the value of interface peak shear stress, but there is no fundamental change in the failure mode of the interface. The interface peak shear stress is mainly influenced by the soil density around the high roughness interface ($R > 10$ mm) and the peak shear stress increases with the initial normal stress increased. If the interface roughness is low ($R < 10$ mm), the interface peak shear stress is mainly influenced by the water content of the interface soils and the peak shear stress may decrease with the increased of initial normal stress.

(2) The interface peak shear stress, shear displacement corresponding to the peak shear stress and the interface initial shear modulus G_0 all decrease with the unloading degree for the same interface roughness R. The interface equivalent friction angle φ increases with roughness increased for the same initial normal stress and the rate of increase is positive with the initial normal stress. The maximum amount of interface shear dilatancy increases with the unloading degree increased, while the maximum amount of interface shear shrinkage decreases with the unloading degree increased for the same interface roughness.

(3) The proposed pile side resistance-displacement model considers both the radial unloading effect and modulus degradation of soil around the pile has been validated by the direct shear tests of 36 groups; The coefficient a takes fixed value of 0.98 and b takes value varies from 0.02 to 0.3 can best fit existing τ–s curves from direct shear tests for different unloading degree and interface roughness.

(4) The effect of radial unloading and interface roughness on the interface mechanical properties can be attributed to the degradation of the equivalent shear modulus G_{eq}, which can be analyzed by a single fitting parameter b. The value of the empirical coefficient b increases with the unloading degree but decreases with interface roughness. Unloading decelerates the degradation of G_{eq} during the early shearing stage (about $\tau < 0.05\tau_f$) and the degradation rate of G_{eq} decreases with the unloading degree increased. After the early shearing stage (about $\tau > 0.05\tau_f$), unloading accelerates the degradation of G_{eq}. However, the increase of interface roughness will accelerate the degradation of G_{eq} during the early shearing stage (about $\tau < 0.05\tau_f$) but decelerate the degradation of G_{eq} after the early shearing stage (about $\tau > 0.05\tau_f$).

REFERENCES

1. Ni, P. P.; Song, L. H.; Mei, G. X.; Zhao, Y. L. (2017) Generalized nonlinear softening load-transfer model for axially loaded piles. *Int. J. Geomech.* 17 [8], 04017019. https://doi.org/10.1061/(ASCE)GM.1943-5622.0000899
2. Guo, W. D. (2001) Pile capacity in nonhomogeneous softening soil. *Soils Found.* 41 [2], 111–120. https://doi.org/10.3208/sandf.41.2_111
3. Seed, H. B.; Reese, L. C. (1957) The action of soft clay along friction piles. *Transactions of the ASCE.* 122 [1], 731–754.
4. Chow, Y. K. (1986) Analysis of vertically loaded pile groups. *Int. J. Numer. Anal. Meth. Geomech.* 10 [1], 59–72. https://doi.org/10.1002/nag.1610100105
5. Chow, Y. K. (1989) Axially loaded piles and pile groups embedded in a cross-anisotropic soil. *Geotechnique.* 39 [2], 203–212. https://doi.org/10.1680/geot.1989.39.2.203
6. Mu, L. L.; Chen, Q. S.; Huang, M. S.; Basack, S. (2017) Hybrid approach for rigid piled-raft foundations subjected to coupled loads in layered soils. *Int. J. Geomech.* 17 [5], 04016122. https://doi.org/10.1061/(ASCE)GM.1943-5622.0000825
7. Randolph, M. F.; Wroth, C. P. (1978) Analysis of deformation of vertically loaded piles. *J. Geotech. Eng. Div.* 104 [12], 1465–1488. https://doi.org/10.1016/0148-9062(79)90663-6
8. Randolph, M. F.; Wroth, C. P. (1979) An analysis of the vertical deformation of pile groups. *Geotechnique.* 29 [4], 423–439. https://doi.org/10.1680/geot.1979.29.4.423
9. Zhang, Q. Q.; Zhang, Z. M. (2011) Study on interaction between dissimilar piles in layered soils. *Int. J. Numer. Anal. Meth. Geomech.* 35 [1], 67–81. https://doi.org/10.1002/nag.893
10. Poulos, H. G.; Davis, E. H. (1968) The settlement behaviour of single axially loaded incompressible piles and piers. *Geotechnique.* 18 [3], 351–371. https://doi.org/10.1680/geot.1968.18.3.351
11. Wang, W.; Yang, M. (2006) An improved elastic analysis method of pile foundation under vertical loading. *Roc. Soil. Mech.* 27 [8], 1403–1406 (in Chinese). https://doi.org/10.3969/j.issn.1000-7598.2006.08.036
12. Xu, K. J.; Poulos, H. G. (2000) General elastic analysis of piles and pile groups. *Int. J. Numer. Anal. Meth. Geomech.* 24 [15], 1109–1138. https://doi.org/10.1002/1096-9853(20001225)24:15%3C1109::AID-NAG72%3E3.0.CO;2-N
13. Ai, Z. Y.; Han, J. (2009) Boundary element analysis of axially loaded piles embedded in a multi-layered soil. *Comput. Geotech.* 36 [3], 427–434. https://doi.org/10.1016/j.compgeo.2008.06.001
14. Cheung, Y. K.; Tham, L. G.; Guo, D. J. (1988) Analysis of pile group by infinite layer method. *Geotechnique.* 38 [3], 415–431. https://doi.org/10.1680/geot.1988.38.3.415

15. Desai, C. S. (1974) Numerical design analysis for piles in sands. *J. Geotech. Eng. Div.* 100 [6], 613–635. https://doi.org/10.1016/0148-9062(74)91242-X

16. Lee, C. Y. (1991) Discrete layer analysis of axially loaded piles and pile groups. *Comput. Geotech.* 11 [4], 295–313. https://doi.org/10.1016/0266-352X(91)90014-7

17. Sheng, D. C.; Eigenbrod, K. D.; Wriggers, P. (2005) Finite element analysis of pile installation using large-slip frictional contact. *Comput. Geotech.* 32 [1], 17–26. https://doi.org/10.1016/j.compgeo.2004.10.004

18. Trochanis, A. M.; Bielak, J.; Christiano, P. (1991) Three - dimensional nonlinear study of piles. *J. Geotech. Eng.* 117 [3], 429–447. https://doi.org/10.1061/(ASCE)0733-9410(1991)117:3(429)

19. Everett, J. P. (1991) Load transfer functions and pile performance monitoring. *Int. J. Roc. Mech. Min. Sciences.* 30 [1], 229–234. https://doi.org/10.1016/0148-9062(93)90572-U

20. Li, Y. H.; Wang, W. D.; Wu, J. B. (2015) Bearing deformation of large-diameter and super-long bored piles based on pile shaft generalized shear model. *Chin. J. Geotech. Eng.* 37 [12], 2157–2166 (in Chinese). https://doi.org/10.11779/CJGE201512004

21. Guo, W. D.; Randolph, M. F. (1997) Vertically loaded piles in non-homogeneous media. *Int. J. Numer. Anal. Meth. Geomech.* 21 [8], 507–532. https://doi.org/10.1002/(SICI)1096-9853(199708)21:8%3C507::AID-NAG888%3E3.0.CO;2-V

22. Zhu, H.; Chang, M. F. (2002) Load transfer curves along bored piles considering modulus degradation. *J. Geotech. Geoenviron. Eng.* 128 [9], 764–774. https://doi.org/10.1061/(ASCE)1090-0241(2002)128:9(764)

23. Lade, P. V.; Duncan, J. M. (1976) Stress-path independent behavior of cohesionless soil. *J. Geotech. Eng. Div.* 102 [1], 51–68.

24. Lambe, T. W. (1967) Stress path method. *J. Soil. Mech. Found. Div.* 93 [6], 309–331.

25. Wang, Z. J.; Xie, X. Y.; Wang, J. C. (2012) A new nonlinear method for vertical settlement prediction of a single pile and pile groups in layered soils. *Comput. Geotech.* 45, 118–126. https://doi.org/10.1016/j.compgeo.2012.05.011

26. Yang, J. J. (2005) Similarity theory and structural model test. *Wuhan University of Technology Press, Wuhan.* (in Chinese)

27. Zhao, C. F.; Wu, Y.; Zhao, C.; Tao, G. X. (2018) Experimental research on the clay-concrete interface shear behaviors considering the roughness and unloading Effect. *Proc. of GeoShanghai 2018 International Conf. Fundamentals of soil behaviours,* 522–530. https://doi.org/10.1007/978-981-13-0125-4_58

28. Dove, J. E.; Jarrett, J. B. (2002) Behavior of dilative sand interfaces in a geotribology framework. *J. Geotech. Geoenviron. Eng.* 128 [1], 25–37. https://doi.org/10.1061/(ASCE)1090-0241(2002)128:1(25)

29. Zhang, G.; Zhang, J. M. (2003) Development and application of cyclic shear apparatus for soil-structure interface. *Chin. J. Geotech. Eng.* 25 [2], 149–153 (in Chinese). https://doi.org/10.3321/j.issn:1000-4548.2003.02.005

30. Zhang, G.; Zhang, J. M. (2004) Experimental study on monotonic behavior of interface between soil and structure. *Chin. J. Geotech. Eng.* 26 [1], 21–25 (in Chinese). https://doi.org/10.3321/j.issn:1000-4548.2004.01.003

31. Fahey, M.; Carter, J. P. (1993) A finite element study of the pressuremeter test in sand using a nonlinear elastic plastic model. *Can. Geotech. J.* 30 [2], 348–362. https://doi.org/10.1139/t93-029

32. Tomlinson, M. J.; Woodward, J. (1977). Pile design and construction practice, Fourth Edition. *A View Point Publications, London.*

33. Chandler, R. J. (1968) The shaft friction of piles in cohesive soils in terms of effective stress. *Civil Eng and Public Works Review.* 63 [738], 48–51.

34. Focht, J.; Vijayvergiya, V. (1972) A new way to predict capacity of piles in clay. *Proc. 4th Offshore Technology Conf.* vol. 2, 865–874. https://doi.org/10.4043/1718-MS

35. Mayne, P. W.; Kulhawy, F. H. (1982) K_0-OCR relationships in soil. *J. Geotech. Eng. Div.* 108 [6], 851–872.

36. Ruiz, M. E. (2005). Study of axially loaded post grouted drilled shafts using CPT based load transfer curves. *Master Thesis, Civil Engineering. University of Puerto Rico.*

37. Mayne, P. W.; Schneider, J. A. (2001) Evaluating axial drilled shaft response by seismic cone. *Foundations and ground improvement, Geotechnical Special Publication.* 113, 655–669.

38. Kulhawy, F. H. (1984) Limiting Tip and Side Resistance : fact or fallacy. *Proc. Conf. on Analysis and Design of Pile Foundations. ASCE Convention, San Francisco, California.* 80–98. https://doi.org/10.1016/0148-9062(86)91224-6

39. Wang, W. B.; Yang, M. (2005) Elasto-plastic analysis for vertical pile based on extended compatibility of deformation. *Chin. J. Geotech. Eng.* 27 [12], 1442–1446 (in Chinese). https://doi.org/10.3321/j.issn:1000-4548.2005.12.014